

# VLBI phase–reference observations of the gravitational lens JVAS B0218+357

Rupal Mittal<sup>1</sup>, Richard Porcas<sup>1</sup>, Olaf Wucknitz<sup>2,3</sup>, Andy Biggs<sup>3,4</sup>, and Ian Browne<sup>5</sup>

<sup>1</sup> MPIfR, Auf dem Hügel 69, 53121 Bonn, Germany

<sup>2</sup> Universität Potsdam, Institut für Physik, Am Neuen Palais 10, D-14469 Potsdam, Germany

<sup>3</sup> JIVE, 7990 AA Dwingeloo, Netherlands

<sup>4</sup> UK Astronomy Technology Centre, Royal Observatory, Edinburgh, U.K.

<sup>5</sup> JBO, Macclesfield, Cheshire SK11 9DL, U.K.

Received/Accepted

**Abstract.** We present the results of phase–referenced VLBA+Effelsberg observations at five frequencies of the double–image gravitational lens JVAS B0218+357, made to establish the precise registration of the A and B lensed image positions. The motivation behind these observations is to investigate the anomalous variation of the image flux density ratio (A/B) with frequency – this ratio changes by almost a factor of two over a frequency range from 1.65 GHz to 15.35 GHz. We investigate whether frequency dependent image positions, combined with a magnification gradient across the image field, could give rise to the anomaly. Our observations confirm the variation of image flux ratio with frequency. The results from our phase–reference astrometry, taken together with the lens mass model of Wucknitz et al. (2004), show that shifts of the image peaks and centroids are too small to account for the observed frequency–dependent ratio.

## 1. Introduction

The radio source JVAS B0218+357 was identified as a gravitationally lensed system by Patnaik et al. (1993). The source (Fig. 1) consists of two compact images, A and B, separated by  $\sim 330$  mas, the smallest angular separation amongst the known galaxy lenses, and a faint Einstein ring of a similar diameter. The lens is identified as a spiral galaxy ( $z \sim 0.684$ , Browne et al. 1993) and the background source, which is conjectured to be a blazar ( $z \sim 0.944$ , Cohen et al. 2003), is variable in its radio emission. An accurate value for the time delay between variations in the images has been measured by Biggs et al. (1999), ( $10.5 \pm 0.4$ ) days (see also Cohen et al. 2000). Previous VLBI observations at high frequencies (Patnaik et al. 1995; Kembell et al. 2001; Biggs et al. 2003) show that both images consist of a compact core component and a secondary compact component, offset by ca. 1.5 mas in the direction of a lower brightness jet of some 15 mas extent. At lower frequencies (e.g. Porcas & Patnaik 1996) the resolution is insufficient to separately resolve the two compact components but the total extent of both images increases considerably with increasing wavelength. In particular, image A, the stronger and larger, is extended in PA  $-40^\circ$ , the expected direction of “tangential stretching”. The wealth of data coming from numerous radio and optical observations of this system at various frequencies and epochs provides constraints for lens models and, together with the time delay, give the possibility to determine the Hubble constant,  $H_0$ .

Yet this system presents a few complications. One of them is the steady and systematic decline in the ratio of radio image flux density of the A and B images with decreasing frequency. This is in direct contradiction to the expected achromatic behaviour of gravitational lensing for point sources. Table 1 lists the observed ratios from previous observations of B0218+357 at various frequencies and times, and using different interferometric instruments. The ratio (A/B) varies from 3.7 to 2.6 over the frequency range 15.35 GHz to 1.65 GHz. At frequencies where the source is variable, the ratio measured at a single epoch will be in error if the timescale for significant variations is comparable with the time delay. The ratios listed from the Biggs et al. (1999) VLA monitoring campaign have been corrected for this effect.

We note that interferometric measurements may underestimate the individual image flux densities if the beam size is much smaller than the extent of the image. If this occurs preferentially in one of the images it will affect the flux ratio; since image A is larger than image B, this effect might decrease the A/B flux ratio. Conversely, insufficient resolution may lead to contamination of the B image by emission from the Einstein ring. We have included entries in Table 1 from short baseline instruments (VLA, MERLIN; marked with an ‘\*’) only at frequencies where the resolution is sufficient to separate the ring emission from image B, to minimize this effect.

Although gravitational lens imaging of a point object is intrinsically achromatic, frequency dependent variations in the image flux ratio of an extended source are possible, provided

**Table 1.** The image flux ratios as a function of frequency. Entries marked with an \* indicate MERLIN and VLA measurements free from contamination by the Einstein ring.

$\nu$ (GHz)	Interferometer	Resolution (mas)	Flux Density: $S^A$ (mJy)	Flux Density: $S^B$ (mJy)	$S^A/S^B$
1.7	VLBI <sup>a</sup>	5	445	170	2.62
5*	MERLIN <sup>b</sup>	50	728	245	2.97
5	EVN <sup>b</sup>	5	660	210	3.14
5	VLBI <sup>a</sup>	1	515	196	2.63
8.4*	VLA <sup>b</sup>	200	767	236	3.25
8.4	VLBI <sup>c</sup>	1.3	$777 \pm 30$	$230.9 \pm 8$	$3.37 \pm 0.17$
8.4	VLBI <sup>a</sup>	1	690	202	3.41
8.4*	VLA <sup>e</sup>	200	–	–	$3.57 \pm 0.01$
15*	VLA <sup>e</sup>	120	–	–	$3.73 \pm 0.01$
15*	VLA <sup>b</sup>	120	698	189	3.69
15.3	VLBA <sup>d</sup>	0.5	$769 \pm 12$	$212 \pm 6$	$3.62 \pm 0.09$

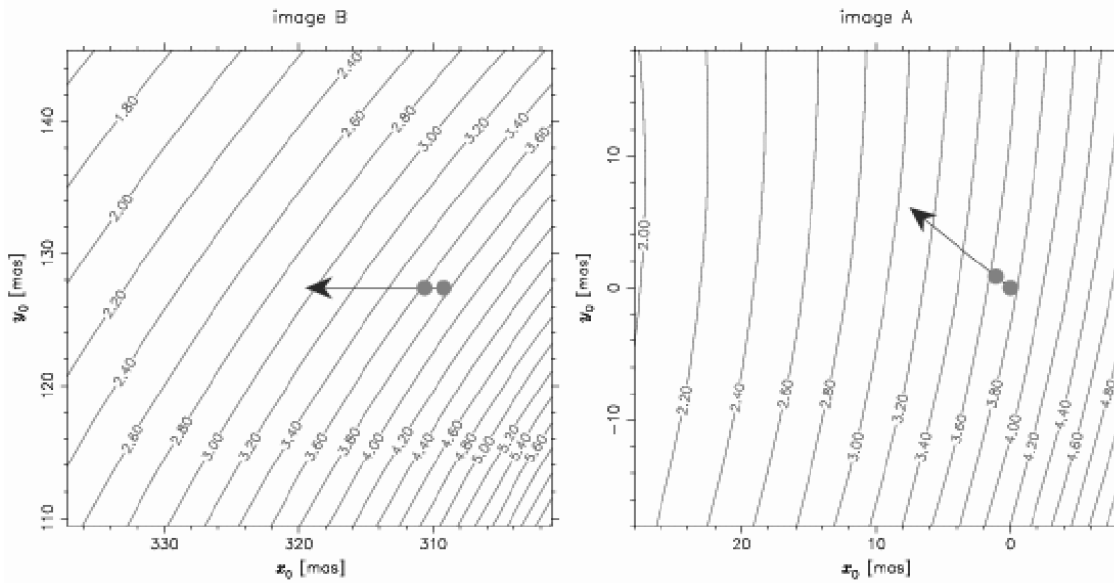
a Patnaik &amp; Porcas (1999)

b Patnaik et al. (1993)

c Kembell et al. (2001)

d Patnaik et al, 1995 (corrected by factor 0.77)

e Biggs et al. (1999) (corrected for flux variability and the time delay; see text)

**Fig. 2.** The curves indicate constant relative magnifications (A/B) for the best fitting lens model with the lens position at  $x_0 = 260$  mas and  $y_0 = 117.5$  mas (Wucknitz 2002).

its structure changes as a function of frequency and extends over regions of different relative magnifications. It seems quite possible that this occurs in B0218+357 since both conditions exist. Firstly, the small image separation leads to relative large changes in magnification across the extent of the images. For simple isothermal ellipsoid models of the lens potential, a shift of 15 mas in the position of a point-source image can produce a change in relative magnification from 4 to 2.5 (see Fig. 2).

Secondly, the frequency-dependence of the B0218+357 image structures is strong, with previous VLBI observations showing a marked increase of image sizes with decreasing frequency. Furthermore, it is common for the radio spectra of one-sided AGN jets such as that seen in B0218+357 to steepen with

distance from the nucleus, providing a natural mechanism for producing a frequency-dependent position. The position of the radio peak at the base of the jet is also expected to move away from the nucleus at lower frequencies - the "core-shift".

However, instrumental limitations prevent these effects from being seen easily. One is the change with frequency of the resolution available from VLBI observations. Another is the loss of absolute position information when phase self-calibration is used to make VLBI maps, which prevents robust registration of maps at different frequencies. Frequency-dependent position shifts should, in general, show up as a change with frequency of the separation between different images (e.g. Porcas & Patnaik 1995). However, such differential

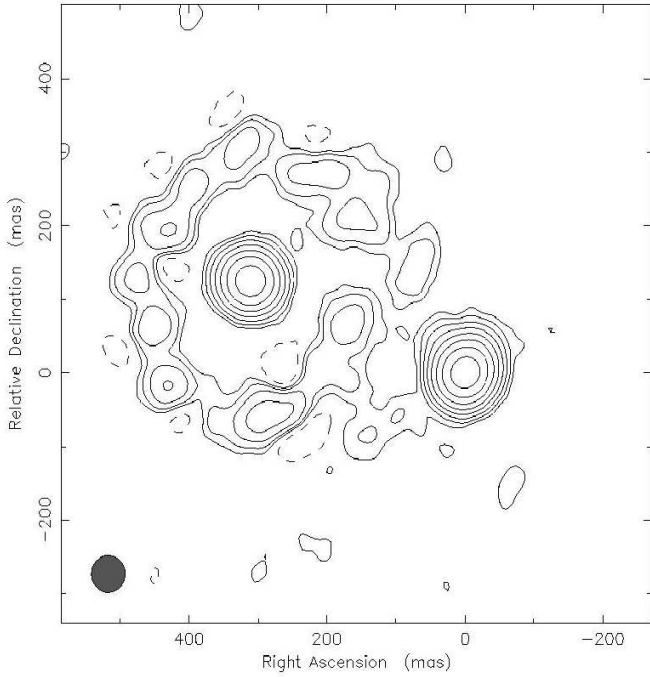


**Fig. 1.** A combined EVN/MERLIN 1.7 GHz map of B0218+357, observed on 29<sup>th</sup> May 1997 (Patnaik et al., unpublished). The resolution of the map is 50 mas and it shows an Einstein ring and the two compact images, A (right) and B (left). The contour levels are  $6.5 \text{ mJy beam}^{-1} \times (-0.5, 0.5, 1, 2, 4, 8, 16, 32, 64)$  and the peak flux density is  $650 \text{ mJy beam}^{-1}$ .

shifts are hard to measure in some cases, especially when the shift is in the same direction in both images. Furthermore, any “feature” (e.g. the core) used to define the positions of the different images may, in fact, include different fractions of the emission in the background source, since the images have different magnifications

In this paper we present the results of phase-referenced VLBI observations of the lens B0218+357, made to establish an unambiguous registration of the structures of the radio images at different frequencies. Although the expected core shifts are relatively small (mas), the positions of the centroids of the image flux density distributions may change with frequency by larger amounts, and these are more representative of the position of the emission. It is therefore important to quantify their changes with frequency when investigating the origin of the frequency-dependent image flux density ratios.

## 2. Phase-Referencing

VLBI observations suffer from the corrupting influence of the troposphere, ionosphere and instrumental uncertainties on the interferometer visibility phase. For observations of strong sources with VLBI arrays, the technique of phase self-calibration can be used. In this the corrupting phases are treated as antenna-based free parameters, which are determined from the measurements using a trial source model (the procedure known as hybrid mapping). However, this is only possible if the signal-to-noise ratio is high when averaging over periods for which the parameters are constant; it cannot be used for

weak sources. Furthermore, the geometrical phases which contain information regarding the source position relative to the antennas, are absorbed in these parameters, resulting in the loss of any information on the source position in the sky.

In phase-referencing an attempt is made to overcome these two disadvantages by determining the corrupting phase errors directly, using observations of a reference source (for a deeper insight see Alef 1989). This source should ideally be point-like, sufficiently strong that phase self-calibration is possible, and close enough to the target source for their tropospheric and ionospheric phase corruptions to be similar. Observations of the target and reference sources are alternated frequently and the phase errors determined from the reference are then interpolated to times at which the (usually weaker) target source is observed. Under the assumption of equal tropospheric, ionospheric and instrumental phase errors for the target and reference sources, these errors can be subtracted from the target, allowing mapping of the target and determination of its position with respect to the reference.

If  $\phi^{\text{tar}}$  and  $\phi^{\text{ref}}$  represent the measured visibility phases for the target and the reference respectively, then,

$$\phi^{\text{tar}} - \phi^{\text{ref}} = (\phi_{\text{str}}^{\text{tar}} - \phi_{\text{str}}^{\text{ref}}) + (\phi_{\text{pos}}^{\text{tar}} - \phi_{\text{pos}}^{\text{ref}}) \quad (1)$$

where the subscripts ‘str’ and ‘pos’ refer to the visibility phase contributions from the intrinsic structures of the target and the reference, and their position errors, respectively.  $\phi_{\text{str}}^{\text{ref}}$  is determined from self-calibration (hybrid) mapping. The last term then represents the difference between the position errors of the target source and the reference; it is constant with frequency only if both sources have achromatic positions.

If the reference source is sufficiently compact that its position is achromatic, it can be considered as an astrometric calibrator. Then, the phase-reference observations can be used to make a correct registration of maps of the target source at different frequencies, to study any frequency-dependent structure.

Although this technique is most often used for mapping faint radio sources, the target in our study, B0218+357, is sufficiently strong ( $\sim 1 \text{ Jy}$ ) that we can use “inverse phase-referencing”. Here, the target is used as the phase-reference for determining the corrupting phases, and phase-reference maps of a point-like, achromatic astrometric reference source are made. One advantage is that relatively faint sources can be used as astrometric references, permitting the choice of sources closer to the target, which minimizes telescope drive times and reduces any difference between the tropospheric and ionospheric phase corruptions of the target and reference. Another advantage is that multiple astrometric reference sources can be used to guard against the possibility that any single one may have chromatic structure.

## 3. Observations

VLBI observations were made at five frequencies, 15.35 GHz, 8.40 GHz, 4.96 GHz, 2.25 GHz and 1.65 GHz, using the NRAO Very Long Baseline Array (VLBA) and the Effelsberg radio telescope (Eb). Two 14 h source tracks were used (13<sup>th</sup> to 14<sup>th</sup> and 14<sup>th</sup> to 15<sup>th</sup> January, 2002) and for each track

**Table 2.** The position references, their separations from B0218+357, the correlated flux density on the short EVN baselines (S-EVN) and on the long EVN baselines (L-EVN) at 5 GHz. The ratio L/S is a measure of source-compactness.

Source name	Separation (degrees)	S-EVN (mJy)	L-EVN (mJy)	L/S
NVSS B0210+366	2.03	127	85	0.66
NVSS B0215+364	1.03	140	86	0.61
NVSS B0222+369	1.30	151	91	0.61

(19 h to 03 h UT for Eb, 19 h to 09 h UT for the VLBA) we switched between two receivers every 22 min. For the first track, observations were alternated between 4.96 GHz and 2.25 GHz/8.40 GHz (S and X dual band) using 1 bit sampling, and for the second track between 1.65 GHz and 15.35 GHz (without Eb) using 2 bit sampling. The data were recorded on four 8 MHz basebands at all the frequencies with the exception of eight basebands at 4.96 GHz. All observations were made in a single (LHC) circular polarization mode, except the dual S/X observations which were made in RHC.

Apart from observing B0218+357, three compact reference sources were observed (see Table 2) along with a fringe finder, B0234+285. Scans on B0218+357 of 1 min 20 s duration were interleaved by scans of 2 min duration on each of the calibrators in succession. The position reference sources were selected from the NRAO VLA Sky Survey (NVSS) catalogue. From an initial sample of candidate sources, these three were found to exhibit flat spectra and the most point-like structure on the basis of EVN and MERLIN 5 GHz observations (Porcas 2001). They all lie within two degrees of B0218+357 and are stronger than 25 mJy at both 1.4 GHz and 5 GHz, with spectral indices flatter than  $-0.47$  (where the flux density,  $S \propto \nu^\alpha$ ;  $\nu$  being the frequency and  $\alpha$  the spectral index).

The data were correlated at the VLBA correlator, with an output averaging time of 2.1 s and a frequency resolution of 0.5 MHz, and further processed in AIPS, the Astronomical Image Processing Software package provided by NRAO.

#### 4. Data analysis and maps

An essential step in the reduction of phase-reference data concerns the assumption of similar tropospheric and ionospheric phase errors for the reference and the target source. For VLBI observations the extra paths through the troposphere and ionosphere are very different for different antennas, especially because the source is seen at different elevations. The mean phase errors due to the troposphere, which scale as  $\lambda^{-1}$ , can be estimated approximately for each antenna, and are taken into account in the model used for correlation. The mean phase errors due to the ionosphere, which scale as  $\lambda$ , are highly unpredictable, however, and thereby prohibit the use of any model at the time of correlation. Since the errors become pronounced at long wavelengths, it is necessary to apply phase corrections from an ionospheric model after correlation. In applying the ionospheric and tropospheric models, it is only the mean phase offset that is removed for every antenna. The terms corresponding to small-scale temporal and spatial fluctuations still remain

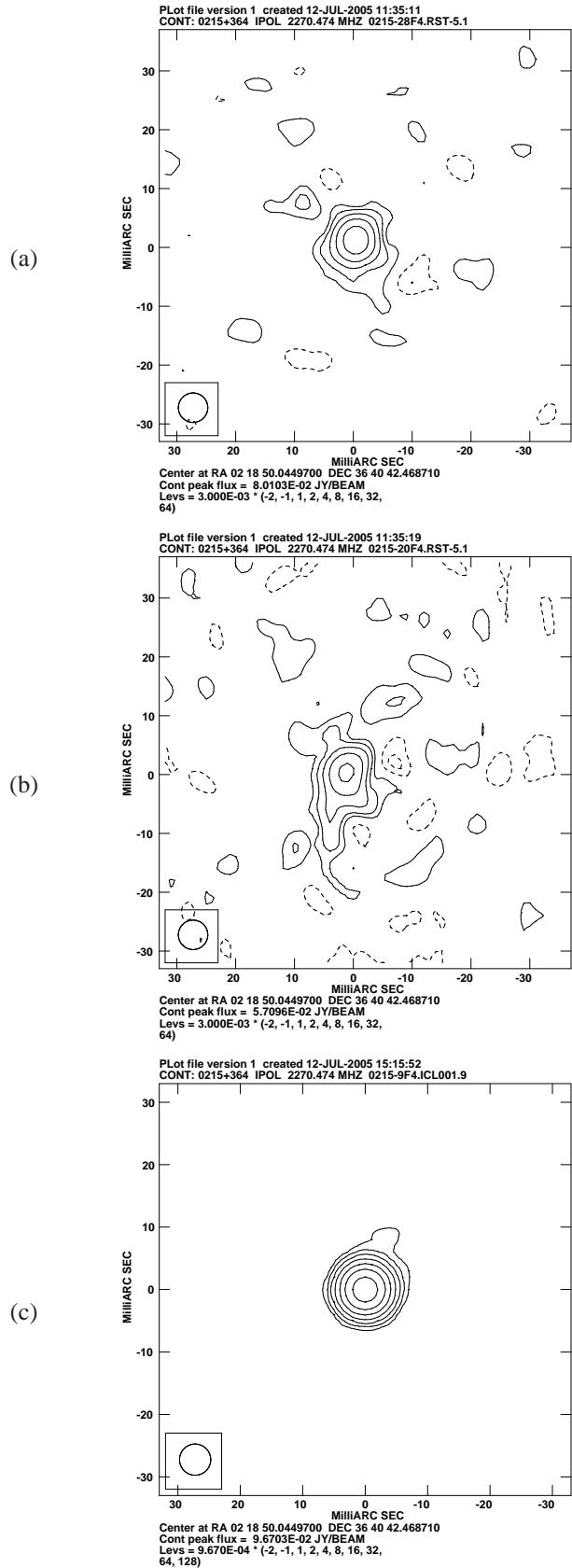


**Fig. 3.** Maps of 0215+364 at 2.3 GHz. a) Inverse phase-referenced map with ionospheric phase calibrations applied to the data. b) Without ionospheric phase calibrations. Both the maps are plotted with a 5 mas restoring beam and with identical contour levels at multiples of 3 mJy c) Hybrid map obtained by means of self-calibration.

and it is hoped they are the same for the target and the reference source. For these observations, we used the AIPS task TECOR to apply an ionospheric model, produced by the Jet Propulsion Laboratory (JPL), and which gives an estimate of the total electron content as a function of longitude, latitude and time (for more details see Walker & Chatterjee 1999).

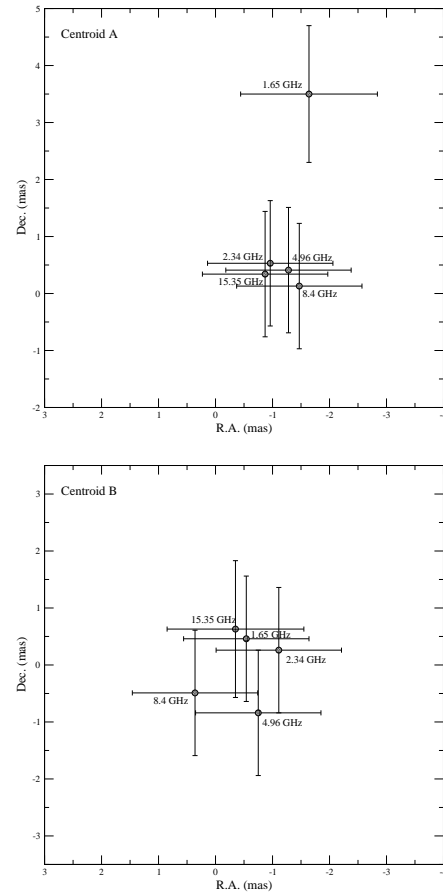
In the further analysis standard reduction procedures were used, applying amplitude calibration derived from telescope radiometry measurements and using fringe-fitting, self-calibration, CLEAN deconvolution procedures and mapping. As mentioned earlier, B0218+357 is sufficiently strong that self-calibration procedures could be applied at all frequencies. Hybrid maps were made by cleaning two sub-fields simultaneously, one for image A and the other for B. After initial maps had been obtained the fringe-fitting was repeated using these as an input model, and the mapping was repeated. Full resolution hybrid maps of both A and B images at all five frequencies are shown in Fig. 4.

All three reference sources also proved to be strong enough to use phase self-calibration, and hybrid maps were therefore also made for these. On inspection, two of these sources were deemed to be unsuitable as position references. For B0210+366 the flux density drops to about 30 mJy at 1.6 GHz and consequently the position of the emission peak is not well defined. The maps of B0222+369 reveal a jet like feature at 2.3 GHz and 1.6 GHz, casting doubt as to whether the position of the peak is achromatic. Therefore for further analysis only B0215+364 was used as a position reference; it appeared point-like in the maps at all frequencies. An amplitude self-calibration procedure was used on this source to determine corrections to the *a priori* amplitude calibration, and these were then applied to the B0218+357 data to improve the maps.

phase-reference maps of B0215+364 were made at all frequencies by applying the self-calibration solutions obtained from B0218+357 to the B0215+364 data. To investigate the efficacy of the ionospheric model we compared phase-referenced images made with and without ionospheric phase corrections. One such comparison can be seen in Fig. 3 which shows maps of B0215+364 at 2.25 GHz. The peak flux per unit beam is almost 1.5 times higher if an ionospheric model is used (Fig. 3(a)). Moreover the peak positions differ by almost half a milliarcsecond. We conclude that even though the rms deviation in the total electron content measured by different groups is of the order of 25 %, the effect of applying any of the models is in the direction that improves the results.

## 5. Results

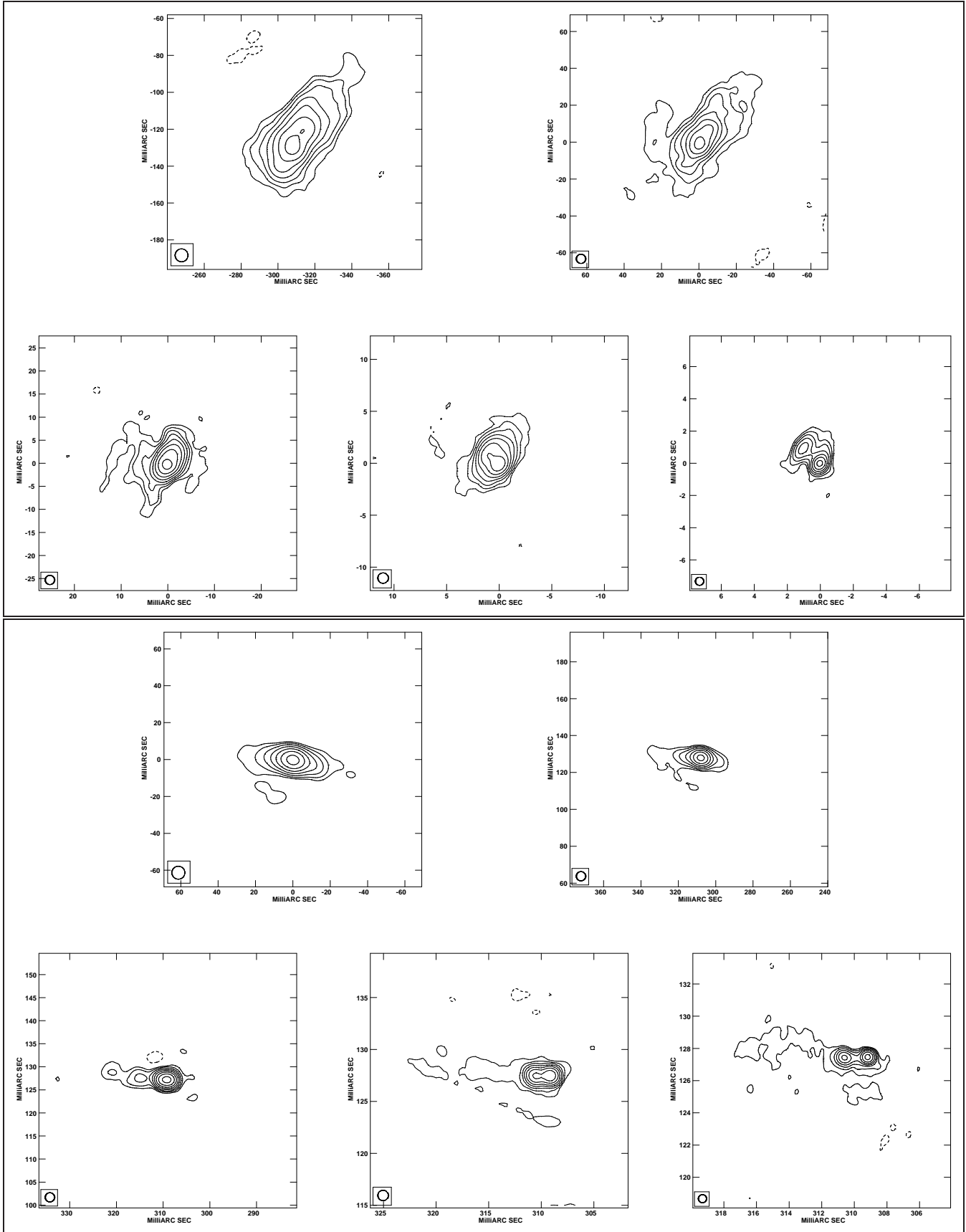
The image flux densities and flux density ratios from these observations are presented in Table 3. To guard against loss of flux density due to over-resolution, we made low-resolution maps by discarding data from the longest baselines (using  $u, v$  resolution cut-offs). The flux densities from these maps were estimated by putting a box around the images and integrating the flux density within the box. The errors on the integrated flux densities given in the table are derived from examining the spread in estimates obtained by varying a number of parameters in the imaging process, and are larger than the formal errors



**Fig. 5.** The change in the centroid position relative to the position-reference B0215+364, at five frequencies in image A (top) and image B (bottom). The error bars at 1.65 GHz, 2.25 GHz and 4.96 GHz are dominated by the position uncertainty in the B0218+357 maps due to the use of relatively large beams, and at 8.4 GHz and 15.35 GHz due to the position uncertainty of B0215+364 caused by the poor dynamic range of the phase-referenced maps at these frequencies.

obtainable from a Gaussian fit. We note that the variation of the image flux density ratio is similar in trend to that found for previous observations, although the range is even larger ( $\sim 4$  to  $\sim 2$ ), with the value at 1.65 GHz differing most from previous estimates. The image A flux density remains almost constant (to within  $\pm 25$  mJy) at the upper four frequencies but drops suddenly by about 130 mJy (20 percent) at 1.65 GHz. In contrast, image B shows a gradual, monotonic increase with wavelength with no sharp drop.

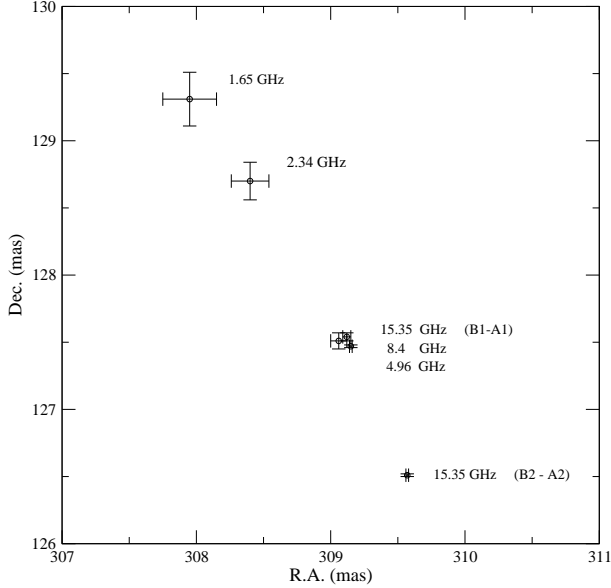
The result of the phase-referenced observations is shown in Fig. 5, which shows the variation with frequency in the centroid position of the radio emission in the images with respect to B0215+364. To determine an image centroid position, the CLEAN components were convolved with a low-resolution restoring beam, and the peak in the resulting map was located using AIPS task MAXFIT, which fits a quadratic function to the brightest area of the map to determine the position offset with respect to the map centre. The same procedure was used to locate the offset from the map centre of the peak position of the calibrator, 0215+364, but using a full-resolution,



**Fig. 4.** The top and bottom panels show 1.65 GHz, 2.25 GHz, 4.96 GHz, 8.40 GHz and 15.35 GHz maps of images A and B respectively, with frequencies increasing from left to right, top to bottom. The residual noise in the maps is  $\leq 500 \mu\text{Jy beam}^{-1}$ . The restoring beams used are (7, 5, 2, 1, 0.5) mas in the order of increasing frequency. The images clearly manifest all the earlier observed lensing-characteristics. Image A is tangentially stretched at a PA  $\sim -40^\circ$  and image B seems to be tangentially compressed. At 8.4 GHz and 15.35 GHz the images reveal further substructure, sub-components 1 and 2 with  $\sim 1.4$  mas separation, representing the core-jet morphology of the background source.

**Table 3.** The image flux density ratios from this data set.

$\nu$ (GHz)	Resolution (mas)	Flux Density: $S^A$ (mJy)	Flux Density: $S^B$ (mJy)	$S^A/S^B$
1.65	50	$495.4 \pm 8.5$	$244.5 \pm 4.3$	$2.03 \pm 0.05$
2.25	50	$629.5 \pm 16.1$	$236.8 \pm 6.6$	$2.66 \pm 0.10$
4.96	30	$641.5 \pm 8.8$	$214.5 \pm 2.5$	$2.99 \pm 0.05$
8.40	10	$673.9 \pm 7.3$	$198.4 \pm 7.3$	$3.40 \pm 0.13$
15.35	5	$665.1 \pm 4.4$	$165.5 \pm 5.4$	$4.02 \pm 0.13$

**Fig. 6.** The A and B separation as a function of frequency. At 15.35 GHz, separations for both the components A1–B1 and A2–B2 are marked and at other frequencies the peak to peak separations are marked.

phase-referenced map. The position of the B0218+357 image centroid with respect to 0215+364 (ignoring the constant position difference used for correlation) is then given by the difference of these offsets (B0218+357 - 0215+364). The same procedure was used for image B. The upper panel of the figure indicates a relative shift of  $\sim 5$  mas in the centroid of image A between 15.35 GHz at 1.65 GHz, although the shift occurs only at 1.65 GHz. For image B, on the contrary, there is no shift detected in the centroid of the brightness distribution. From the Singular Isothermal Elliptical Potential (SIEP) model (Fig. 2), we find that a shift of 5 mas may cause the flux ratio to change as much as  $\sim 0.5$ , and looking at Table 3, this corresponds to  $\sim 12.5\%$  change in the observed flux ratio. However, this depends upon the direction in which the shift has occurred. From the phase-referenced results for image A, we infer that this direction roughly coincides with the constant relative magnification contours (more or less tangential with respect to the lens centre) and this shift corresponds to  $\leq 6\%$  change in the observed ratio. Therefore we draw the conclusion that the measured shift with frequency of either image centroid

positions is not sufficient to account for the flux ratio anomaly for B0218+357.

An advantage of imaging gravitational lenses is that any frequency-dependent position in the source can be seen as a frequency-dependence of the separation vector of the lensed images, without requiring the use of an external reference source. As mentioned in Section 1, this method is insensitive in cases where the position shift is along the same direction in both the images, but the accuracy of the measurement of the A–B separation is much higher than for that between B0218+357 and B0215+364. A–B separations at different frequencies, measured with MAXFIT in full resolution maps, are shown in Fig. 6. Since the images at 15.35 GHz are resolved into sub-components 1 and 2, the separations of both A1–B1 and A2–B2 are indicated in the plot. For the other frequencies it is the peak to peak separation that is shown. We see that the separation at 15.35 GHz (A1–B1), 8.4 GHz and 4.96 GHz remains roughly the same implying that the “peak” is centred around component 1 in both the images. At 2.25 GHz and 1.65 GHz, the separation increases in declination and decreases in right ascension, in contrast to the behaviour of component 2. This is surprising as one might expect the separation at lower frequencies to gradually coincide with the A2–B2 separation, reflecting relatively more prominent emission from component 2 at the base of the jet. We note that the (less accurate) 1.65 GHz centroid separation is indeed greater in declination than at other frequencies, as for component 2.

At 1.65 GHz we identify another component in image A, separated by  $\sim 10$  mas from component 1 and  $\sim -33^\circ$  P.A., shown in Fig. 7(a). The origin of this newly-identified feature (hereon component 3) is of great interest and we have investigated how this can be part of the background source. On applying the lens model by Wucknitz et al. (2004), we deduce in image B it should be  $\sim 3$  mas from component 1 as indicated in Fig. 7(b). Unfortunately the resolution at this frequency is not enough ( $\sim 7$  mas) to resolve this separation. Therefore even though there is no hint of component 3 in image B (as one can conclude from the rather smooth contour curves around component 1 and the slice cut shown in Fig. 7(d)), we cannot distinguish whether this is a distinct feature in the background source imaged in A by the smooth macro potential of the lens, or whether it is caused by some other mechanism. The shift in the centroid position of image A at 1.6 GHz may be attributed to the existence of component 3.

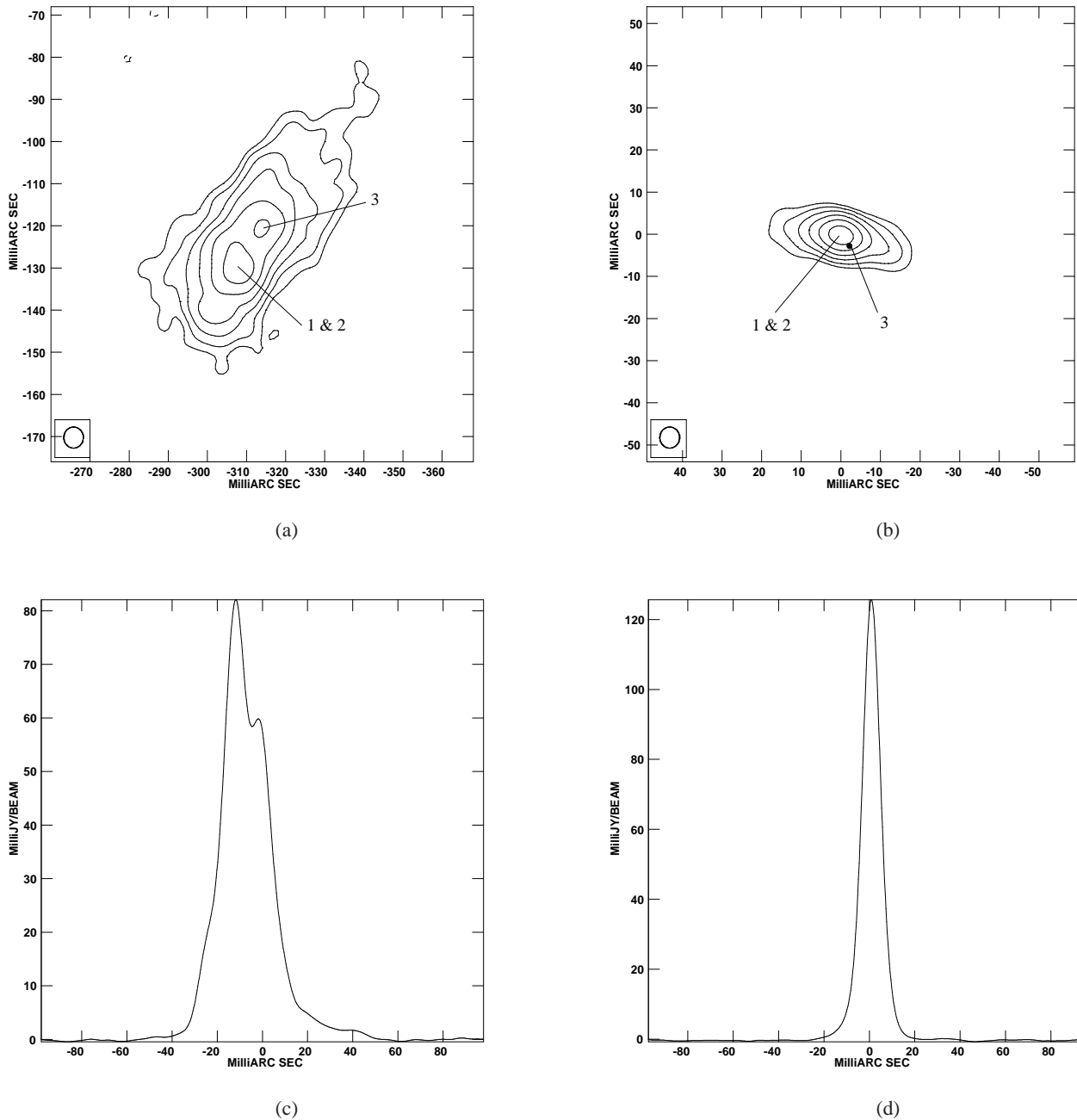


**Fig. 7.** a) Second maximum (component 3) detected at 1.65 GHz in image A at a separation of  $\sim 10$  mas from component 1 & 2 (The components 1 and 2 are not resolvable at these frequencies, hence what is marked is their superposition). b) The predicted position of component 3 in image B at 1.65 GHz, marked as a black dot about  $\sim 3$  mas from component 1 & 2. The resolution at this frequency is about 7 mas. c) A slice through the components 1 & 2 and 3 in image A. d) A slice through the components 1 & 2 and the expected position of component 3 in image B.

## 6. Discussion

We have successfully used the technique of inverse phase-referencing to investigate the frequency-dependence of the emission from the images of B0218+357; we believe this is the first time in which a gravitational lens has been used as a phase-reference. We have established the change in the centroid position of the image brightness distributions over five frequencies, and also investigated the change in the positions of the emission

peaks using inter-image astrometry. The shift in the centroid in image A, which is significant ( $\sim 5$  mas) only at 1.65 GHz, is in a direction along which the relative magnification is predicted to be constant. In image B no significant frequency dependent shift is detected in the position of the centroid. A reasonable assumption is that the relative image magnification at the centroid positions derived from the model gives a good measure of the expected image flux density ratio. Thus we conclude that

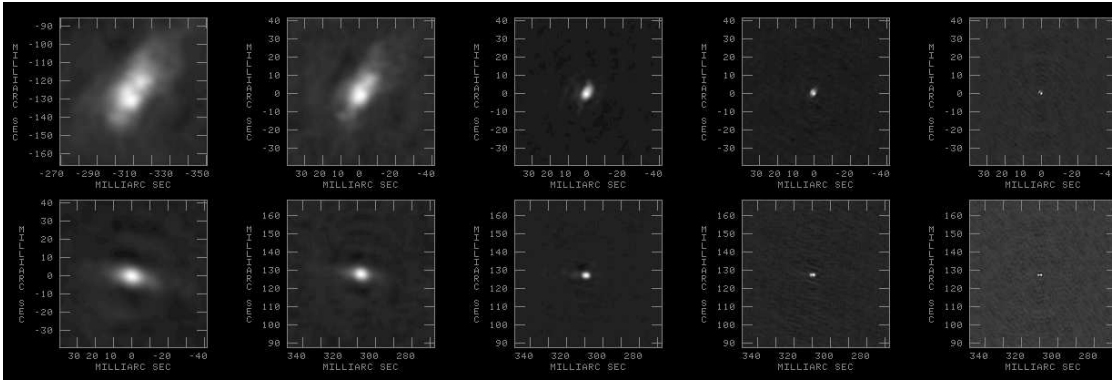


**Fig. 8.** Image A (top) and image B (bottom) at 1.65 GHz, 2.25 GHz, 4.96 GHz, 8.40 GHz, 15.35 GHz (from left to right) plotted with the same scale. The beam size is (5, 4, 2, 1, 0.5) mas respectively and each side of the square measures 80 mas.

the changing magnification gradient across the images is not the main cause of the anomalous change of image flux density ratio with frequency.

Fig. 8 shows images A and B plotted with the same scale at all the frequencies. As can be clearly seen, at 1.65 GHz there is a huge amount of low brightness emission that extends out to  $\sim \pm 30$  mas. In comparison, at 15.35 GHz the emission is dominated by the compact sub-components with a separation of  $\sim 1.4$  mas. At lower frequencies the (larger) images extend over regions where lens models do, indeed, predict significant changes in the relative magnification, and it may be insufficient to simply consider magnifications at the centroid positions. This is because low frequency emission from different regions of the background source is magnified by very different amounts. The resultant average magnification is thus the integral of the (background source) intensity-weighted magnification over the image area.

We plan to extend our study by applying the model from LensClean and evaluating the ratio of the (background source) intensity-weighted magnifications of image A to B, explicitly taking the observed extension of the background source into account. We also want to extend our choice of lens model to one with a non-isothermal mass-radius profile. The motivation for this is the observation by Biggs et al. (2003) related to the jet stretching factor, which seems to be larger in image B than A, as seen when projected back to the source plane. But the deviation from non-isothermality is expected to be small (Wucknitz et al. 2004) since low-resolution VLA observations of the Einstein ring are fitted quite well with isothermal models.

The identification of a distinct secondary maximum in image A at low frequencies (component 3), the sharp downturn in the spectrum of image A at 1.6 GHz (not visible in image B) and the small shift in the 1.6 GHz peak position in A are further results from these observations with no obvious explanation in terms of the expected magnification gradients across the images. It may, therefore, be necessary to consider more elaborate mechanisms (mass sub-structure, free-free absorption or refractive scattering in the lens galaxy) to account for all the observed features in the B0218+357 images.

*Acknowledgements.* We thank Martin Kilbinger for useful suggestions and critiques. We appreciate Peter Schneider for his timely discussions. We would like to thank the VLBA and Effelsberg opera-

tional staff, and the VLBA correlator staff for their help in obtaining the data. The National Radio Astronomy Observatory is a facility of the National Science Foundation operated under cooperative agreement by Associated Universities, Inc. The Effelsberg radio telescope is operated by the Max-Planck-Institut für Radioastronomie (MPIfR). R. M. is supported by the International Max Planck Research School (IMPRS) for Radio and Infrared astronomy at the Universities of Bonn and Cologne.

## References

- Alef, W. 1989, in *Very Long Baseline Interferometry, Techniques and Applications*, NATO ASI Series C: Mathematical and Physical Sciences, ed. M. Felli & R. E. Spencer, Vol. 283, 261
- Biggs, A. D., Browne, I. W. A., Helbig, P., et al. 1999, *MNRAS*, 304, 349
- Biggs, A. D., Wucknitz, O., Porcas, R. W., et al. 2003, *MNRAS*, 338, 599
- Browne, I. W. A., Patnaik, A. R., Walsh, D., & Wilkinson, P. N. 1993, *MNRAS*, 263, L32
- Cohen, A. S., Hewitt, J. N., Moore, C. B., & Haarsma, D. B. 2000, *ApJ*, 545, 578
- Cohen, J. G., Lawrence, C. R., & Blandford, R. D. 2003, *ApJ*, 583, 67
- Kemball, A. J., Patnaik, A. R., & Porcas, R. W. 2001, *ApJ*, 562, 649
- Patnaik, A. R., Browne, I. W. A., King, L. J., et al. 1993, *MNRAS*, 261, 435
- Patnaik, A. R. & Porcas, R. W. 1999, in *ASP Conf. Ser. 156: Highly Redshifted Radio Lines*, ed. C. L. Carilli, S. J. E. Radford, K. M. Menten, & G. I. Langston, 247–251
- Patnaik, A. R., Porcas, R. W., & Browne, I. W. A. 1995, *MNRAS*, 274, L5
- Porcas, R. W. 2001, in *15th Working Meeting on European VLBI for Geodesy and Astrometry*, 201–207
- Porcas, R. W. & Patnaik, A. R. 1995, in *10th Working Meeting on European VLBI for Geodesy and Astrometry*, 188–192
- Porcas, R. W. & Patnaik, A. R. 1996, in *IAU Symp. 173: Astrophysical Applications of Gravitational Lensing*, ed. C. S. Kochanek & J. N. Hewitt, 311–316
- Walker, C. & Chatterjee, S. 1999, *VLBA Scientific Memo*, 23
- Wucknitz, O. 2002, Ph.D. Thesis, University of Hamburg

Wucknitz, O., Biggs, A. D., & Browne, I. W. A. 2004,  
MNRAS, 349, 14